Multimodal Encapsulation to Selectively Hydrogen and Engineer Channel Conduction for p-type SnO_x Thin Film Transistor Applications

Dong Hun Lee^{1,#}, Yuxuan Zhang^{1,#}, Sung-Jin Chang², Honghwi Park³, Chung Soo Kim⁴, Jinwook Baek¹, Jeongmin Park⁴, Kwangsoo No⁵, Han Wook Song⁶, Hongsik Park³, and Sunghwan Lee^{1,*}

Keywords: p-type oxides; SnO_x; thin film transistors; doping mechanism; encapsulation; selective permeation; hydrogen doping

¹ School of Engineering Technology, Purdue University, West Lafayette, IN 47907, USA

² Center for Analysis & Evaluation, National Nanofab Center, Daejeon 34141, Republic of Korea

³ School of Electronic and Electrical Engineering, Kyungpook National University, Daegu 41566, Republic of Korea

⁴ Analysis Technical Center, Korea Institute of Ceramic Engineering and Technology, Jinju, Gyeongsangnam-do 52851, Republic of Korea

⁵ Department of Materials Science and Engineering, KAIST, Daejeon 34141, Republic of Korea

⁶ Center for Mass and Related Quantities, Korea Research Institute of Standard and Science, Daejeon 34113, Republic of Korea

^{*}Corresponding authors: sunghlee@purdue.edu

[#]These authors contributed equally to this work.

Abstract

It has been challenging to synthesize p-type SnO_x (1 $\leq x\leq 2$) and engineer the electrical properties such as carrier density and mobility due to the narrow processing window and the localized oxygen 2p orbitals near the valence band. Herein, we report on the multifunctional encapsulation of p-SnO_x to limit the surface adsorption of oxygen and selectively permeate hydrogen into the p-SnO_x channel for thin film transistor (TFT) applications. Time-of-flight secondary ion mass spectrometry (ToF-SIMS) measurements identified that ultra-thin SiO₂ as a multifunctional encapsulation layer effectively suppressed the oxygen adsorption on the back channel surface of p-SnO_x and selectively diffused hydrogen across the entire thickness of the channel. Encapsulated p-SnO_x-based TFTs demonstrated much-enhanced channel conductance modulation in response to the gate bias applied, featuring higher on-state current and lower offstate current (on/off ratio $> 10^3$), field effect mobility of 3.41 cm²/Vs and threshold voltages of ~5-10 V. The fabricated devices show minimal deviations as small as $\pm 6\%$ in the TFT performance parameters, which demonstrates good reproducibility of the fabrication process. The relevance between the TFT performance and the effects of hydrogen permeation is discussed in regards to the intrinsic and extrinsic doping mechanisms. Density functional theory calculations reveal that hydrogen-related impurity complexes are in charge of the enhanced channel conductance with gate biases, which further supports the selective permeation of hydrogen through a thin SiO₂ encapsulation.

1. Introduction

Oxide electronics have gained prominence in recent years and have been established as one of the most promising new technologies for next-generation displays^{1, 2}, chemical sensors³, energy efficient neuromorphic computing^{4, 5}, and oxide-based bipolar structures such as p-n junctions⁶. The high potential use seen in oxide electronics is primarily due to their high carrier mobilities and their ability to be fabricated at low temperatures. However, the vast majority of oxide semiconductors are n-type oxides, which limits the current applications to unipolar devices and ultimately stunts the development of bipolar devices^{7,8}. Due to the nature of oxides and their relationship with oxygen, oxygen vacancies are the predominant defect, particularly for non-stoichiometric oxides⁹. To maintain charge neutrality, the formation (or annihilation) of oxygen vacancies generates (or consumes) two electrons per vacancy, which is the governing native defect-based doping mechanism in oxide-based semiconductors such as intrinsic and doped forms of ZnO, ¹⁰ In₂O₃, ^{9, 11} TiO₂, ¹², and other metal oxide semiconductors¹³.

Recently, we reported on the processing of p-type SnO_x and oxide-based p-n heterostructures, demonstrating a high on/off rectification ratio (>10³), small turn-on voltage (<0.5 V), and low saturation current (~1×10⁻¹⁰ A).⁶ In general, the growth conditions for p-type SnO_x (1<x<2) are believed to be extremely narrow^{8, 14} due to the formation of SnO_2 (n-type)^{8, 14} and the precipitation of metallic Sn^8 . Although we have reported on the synthesis of sputter-processed p-type SnO_x devoid of metallic Sn, we indeed noticed that the processing window is critically sensitive to the oxygen potential during the process and no p-type behaviors are observed beyond the oxygen potential of 10-14 % in the sputter gas of an Ar/O_2 mixture. The issue of the narrow processing window of p- SnO_x is supported by a recent study from Barros *et al.*¹⁵, in which only

limited oxygen partial pressures (O_{pp}) of 2.8-3.8% from an Ar/O₂ mixture result in p-type conduction after annealing room temperature-processed SnO_x films at 200 °C. In addition, they also reported that O_{pp} during the sputtering process plays a significant role in the resulting crystalline structure, presence of additional Sn-related phases, optoelectronic properties, and hence the TFT performance. Within the O_{pp} range, higher O_{pp} deposition conditions lead to stronger diffraction intensity from the p-SnO_x (101) orientation, higher optical transparency, and larger bandgap (both direct and indirect), compared to those processed at lower O_{pp} ¹⁵. In order to further understand the p-type oxide and engineer the properties for various electronic device applications, it is important to identify the dominant doping and transport mechanisms. The low dopability in p-type SnO_x, of which the causation is also closely related to the narrow processing window, is another challenging issue to adequately engineering the electrical properties of the material^{16, 17}.

The mechanism of native (or intrinsic) defect doping in p-type oxides has not been fully established but, the origin of p-type conductivity of SnO_x (1<x<2) is likely attributed to the excess oxygen in the stoichiometric ratio of O/Sn, i.e., greater than one (unity). The excess oxygen condition is attained by either oxygen interstitials $(O_i'')^{18-20}$ or Sn vacancies $(V_{Sn}'')^{18-21}$. In the presence of oxygen interstitials, the creation of a negatively charged oxygen interstitial donates two holes per interstitial, which contributes to the native p-type doping in SnO_x by the equilibrium defect equation:

$$\frac{1}{2}O_2 = O_i" + 2h^{\bullet} \tag{1}$$

where the inclusion of an oxygen interstitial in the SnO lattices generates two holes to maintain charge neutrality. This oxygen interstitial-based doping mechanism was supported by several previous studies^{18, 22-24}. For example, Ou *et al.*¹⁸ attributed the p-type behavior of p-SnO_x to oxygen interstitials (O_i ") based on their air-annealing (i.e., oxidizing environment) study. The oxygen interstitial mechanism in p-SnO_x is endorsed by previous reports^{22, 24-26} that the open structure of layered SnO allows a range of oxygen interstitials leading to the p-type condition in SnO_x.

Other studies^{21, 27-29}, for instance by Fortunato *et al.*, Togo *et al.*, and Yabuta *et al.*, suggested that the Sn vacancy is the favorable defect under oxygen-rich conditions by the defect equation: $Sn_{Sn}^{x} = Sn + V_{Sn}" + 2h^{\bullet}$ (2)

where the creation of an Sn vacancy on the Sn sublattice liberates two holes. The Sn vacancy mechanism is further supported by the notion that the formation of cation vacancy is likely easier than the inclusion of oxygen interstitials²⁷. However, another computational study by Van de Walle *et al.* reported³⁰ that due to the high formation energy, Sn vacancies are unlikely to form and therefore, difficult to be the dominant acceptor (i.e., dopant) in p-SnO_x.

In addition to the native defect-based (intrinsic) doping mechanisms, extrinsic doping of p-SnO_x was also considered to engineer the carrier density for electronic device applications. Several cations such as Mn, Y, and Al ions were incorporated to reduce the oxygen stoichiometry in SnO₂ through such low-valent ion states of the dopants, and then to achieve p-SnO_x (1<x<2)³¹⁻³³; however the resulting material may include mixed phases of p-type and n-type tin oxides with ambipolar behaviors. Moreover, the chemical reduction strategy was more focused on the synthesis of p-type oxides and was not favored to engineer the carrier density in the resulting material. On the other hand, several studies reported that hydrogen could also work as an efficient extrinsic dopant in p-SnO_x. Hydrogen is known as a common impurity in semiconductors and is found in general growth and processing environments such as ambient air where H₂ or H₂O reside ^{34, 35}. It has been reported that intentional and/or unintentional hydrogen

incorporation in oxide semiconductors works as dopants for both n-type and p-type oxides due to the oxygen reduction ability and defect passivation capability (leaving positively charged defect complex) of hydrogen, respectively ^{11, 30, 36}. Particularly, the unintentional presence of hydrogen in p-SnO_x was reported experimentally by Nomura et al. ³⁶ and theoretically by Van de Walle et al. 30. In a recent Rutherford backscattering/Hall scattering factor study, Nomura et al. 36 identified a relatively high density of hydrogen as high as $\sim 5 \times 10^{19}$ /cm³ in the entire thickness of as-deposited p-SnO_x films prepared with PLD, where no hydrogen or related sources were employed during the process. After annealing in a hydrogen-contained atmosphere (H₂ 5%), the hydrogen concentration was further increased to 8.5x10²⁰ /cm³, which was identified to passivate the defect states and enhanced the TFT performance. A density functional theory (DFT) study on the electronic structure and defect physics of p-type SnO_x by Van de Walle et al. also suggested unintentional hydrogen incorporation responsible for the p-type behavior in SnO_x by forming defect complexes with Sn vacancies that still work as shallow acceptors (i.e., p-type dopant) in SnO_x ³⁰. Although the origin of unintentional hydrogen incorporation has not been fully established yet, in both experimental and theoretical studies, in general, H₂ and/or H₂O in air are the attributes, which is likely included unintentionally during the deposition processing^{30, 36}.

To be an effective p-type dopant in p-SnO_x, the suggested defects and mechanisms for hydrogen incorporation require low formation energy near the valence band maximum, however inconsistent defect forms were identified as dominant dopants through theoretical studies based on atomistic scale calculations, depending on the selection of functional employed³⁰. Some suggested that doped hydrogen is present as an interstitial dopant³⁷ while others proposed defect complexes where hydrogen forms bonding with native point defects (e.g., oxygen or Sn

vacancies)³⁸⁻⁴⁰, where the hydrogen in defect complexes is considered defect passivating agents, contributing stability and reliability of p-SnO_x ⁴¹. Although possible hydrogen doping in p-SnO_x was recently suggested, it requires further validations through direct experimental evidence^{30, 40, 42}. Overall for the doping mechanisms in p-SnO_x, the formation mechanisms of shallow acceptors within the bandgap and hence the doping behaviors are not fully established yet.

The engineering of carrier density of the promising p-type oxides is essential to ensure a reasonable on/off ratio, low off-state current, and threshold voltages for practical electronic and optoelectronic devices such as TFT channel and bipolar logic applications. Therefore, establishing strategies for tuning the carrier density in p-SnO_x is required with a fundamental understanding of the intrinsic and extrinsic doping mechanisms. The overarching goal of this study is to engineer the carrier density of p-SnO_x by identifying dominant intrinsic and available extrinsic doping mechanisms for TFT channel applications. To this end, TFTs with pristine and surface-encapsulated p-SnO_x channels were fabricated and their device performance was compared. X-ray photoelectron spectroscopy (XPS) and time-of-flight secondary ion mass spectroscopy (ToF-SIMS) were used to evaluate the chemical environment of the valence states of the major elements and their distribution across the channel p-SnO_x. To complement the experimental investigations, density functional theory (DFT) calculations were also conducted. In addition to the native defect-based doping mechanisms for p-SnO_x, which are thus far controversial and limited due to the narrow processing windows, possible extrinsic doping strategies will also be discussed. Particularly, the feasibility of hydrogen doping in the presence of SiO₂, its favorable defect structure, and the effect on the TFT performance will be focused on by comparisons of TFT performance and DFT calculations.

2. Experimental

P-type SnO_x films were prepared on Si and glass substrates using dc magnetron sputtering from a high purity Sn target (99.999%, Kurt J. Lesker) at a dc power of 30W, at a substrate rotation rate of 5 rpm, and at Ar/O₂ sputter gas ratios of 86/14 and 90/10 as reported earlier in our previous studies.⁶ In order to limit the inhomogeneous plasma and thermal conditions during the sputtering process, samples were placed on the same spots on a rotating stage (rotation rate of 5 rpm) during the sputtering process, which also minimizes the deviations in the resulting film properties from batch to batch. Film sputter depositions were conducted after achieving a chamber base pressure at 3-5×10⁻⁷ Torr and a 5-10 min pre-sputter process to ensure high vacuum conditions and low-contaminant surfaces of sputter targets, respectively. The resulting SnO_x films were then annealed in air at 300 °C to achieve the stable crystalline state of p-SnO_x. The resulting crystalline structure remains stable in the air ambient conditions even after 10 h annealing at 300 °C. Encapsulation SiO₂ films from a sintered SiO₂ target (99.995%, Kurt J. Lesker) were deposited using rf sputtering at an rf power of 100W with pure Ar sputter and mixed Ar/O₂ gas conditions, and other parameters were the same as those of the SnO_x process.

Thicknesses of the resulting p-SnO_x and SiO₂ films were measured with an FS-1 multiwavelength ellipsometer (FilmSense) at an incident and detection angle of 65°. The chemical and electronic valence states of the major elements in the p-SnO_x films deposited on Si were evaluated in a Thermo Fisher Scientific NEXSA XPS spectrometer. XPS measurements were performed under an ultra-high vacuum of approximately 5×10^{-8} Torr with focused monochromatic soft Al $K\alpha$ x-ray radiation at 1486.6 eV. A UV-Vis-NIR spectrometer (Varian

Cary 5000) was used to investigate the optoelectronic properties of the p-SnO_x thin films (grown on glasses) in the wavelength regime of 300-2500 nm. To exclude the substrate glass information in the resulting UV-Vis-NIR spectra, a reference bare glass was used for a baseline scan. Crystallographic diffraction structures were measured in an X-ray diffractometer (Malvern Panalytical Empyrean) through a θ -2 θ coupled scan mode with Cu $K\alpha$ radiation (λ = 1.54 Å) at operation conditions of 45 kV and 40 mA. Transmission electron microscopic (TEM) images were obtained through an FEI Themis Z TEM microscope to investigate the cross-sectional structure of specimens. Elemental mapping analysis was conducted with an energy dispersive Xray spectrometer (EDS), attached to the FEI Themis Z TEM microscope. The EDS mapping is particularly to identify the presence of ultra-thin encapsulation SiO₂ (3-4 nm). For TEM sample preparation, a focused ion beam system (Helios G4 UC, ThermoFisher Scientific) was used. ToF-SIMS measurements were conducted using an M6 (IONTOF GmbH, Münster, Germany) instrument with Bi⁺ primary ions as the analysis beam at an energy of 30 keV. For the depth profiling of secondary ions of interest on the same point on samples, Cs⁺ ions with an energy of 250 eV were used as the sputtering beam for positive secondary ions detection. The analyses with the Bi⁺ beam were performed over a $100 \times 100 \, \mu \text{m}^2$ area (32 × 32 pixels), located in the center of the $400 \times 400 \ \mu m^2$ etching crater created by the Cs⁺ sputter beam. The sputtering rates of the p-SnO_x and SiO₂ film samples were approximately 0.019 nm/s and 0.015 nm/s, respectively. These values were used to convert sputtering time into depth profiles of the samples.

Bottom-gated TFT devices based on the p-SnO_x channel were fabricated, where thermally grown SiO₂ (300 nm) was used at the gate dielectric, and heavily-doped Si (0.003–0.005 Ω cm) was

commonly used as the gate and the substrate. Channel and source/drain metallization patterns were defined using shadow masks. For metallization, Sn was sputter-deposited to a thickness of approximately 75 nm. Some p-SnO_x TFTs employed a thin SiO₂ layer (3-4 nm) to passivate the back-channel region of the TFTs to evaluate the effect of SiO₂ on the TFT performance. A semiconductor parameter analyzer (Agilent 4155B) was used to characterize the p-SnO_x TFT performance (with and without SiO₂) in a dark probe station under ambient air conditions, for which the devices were rested for at least 20 minutes in the light-tight probe station in order to minimize the effect of photoconductivity in the p-SnO_x channel. More than 80 devices were fabricated and tested to gather reliable results and provide evidence of reproducibility. Devices with six different aspect ratios (width/length, W/L) of 2000/200, 2000/150, 2000/100, 1000/200, 1000/150, and 1000/100 in μm/μm were fabricated on a single wafer. The fabricated devices show approximately ±6% deviations in the TFT performance parameters such as field effect mobility, which demonstrates good reproducibility of the fabrication process. It has been reported⁴³⁻⁴⁵ that the contact resistance (2R_C) at the channel/metallization interface and its modulation may underestimate the field effect mobility of oxide-based TFTs, particularly with the channel length, L shorter than 50 µm while no significant mobility underestimation was found in TFTs with $L > 50 \mu m$ since the contribution of $2R_C$ to the total resistance ($R_T = 2R_C + R_{ch}$, where R_{ch} is the channel resistance) is much less than that of the R_{ch} in long channel TFTs. The channel length evaluated in this study ranges from 100-200 µm and, therefore, the effect due to the global bottom gate on the field effect mobility is expected to be minimal.

First-principles calculations were performed within the generalized Kohn-Sham theory with the screened hybrid functional of Heyd, Scuseria, and Ernzerhof (HSE) and using the projector

augmented-wave method as implemented in Quantum Espresso⁴⁶. The supercells for defect calculations were constructed from the 8 (2×2×2) unit cells, which correspond to 32 atoms in a perfect crystal. For charged defects, a jellium background was employed to neutralize the supercells. The typical space-group of SnO, P4/nmm (SG129) which is the litharge crystal structure was considered for the calculations. The lattice constants of a=b=7.7412 Å and c=10.0505 Å were used based on the optimized unit-cell geometry. The k point was sampled at the Γ point and the force and energy convergence criterion were set to 0.02 eV/Å and 10^{-5} eV, respectively.

3. Results and discussion

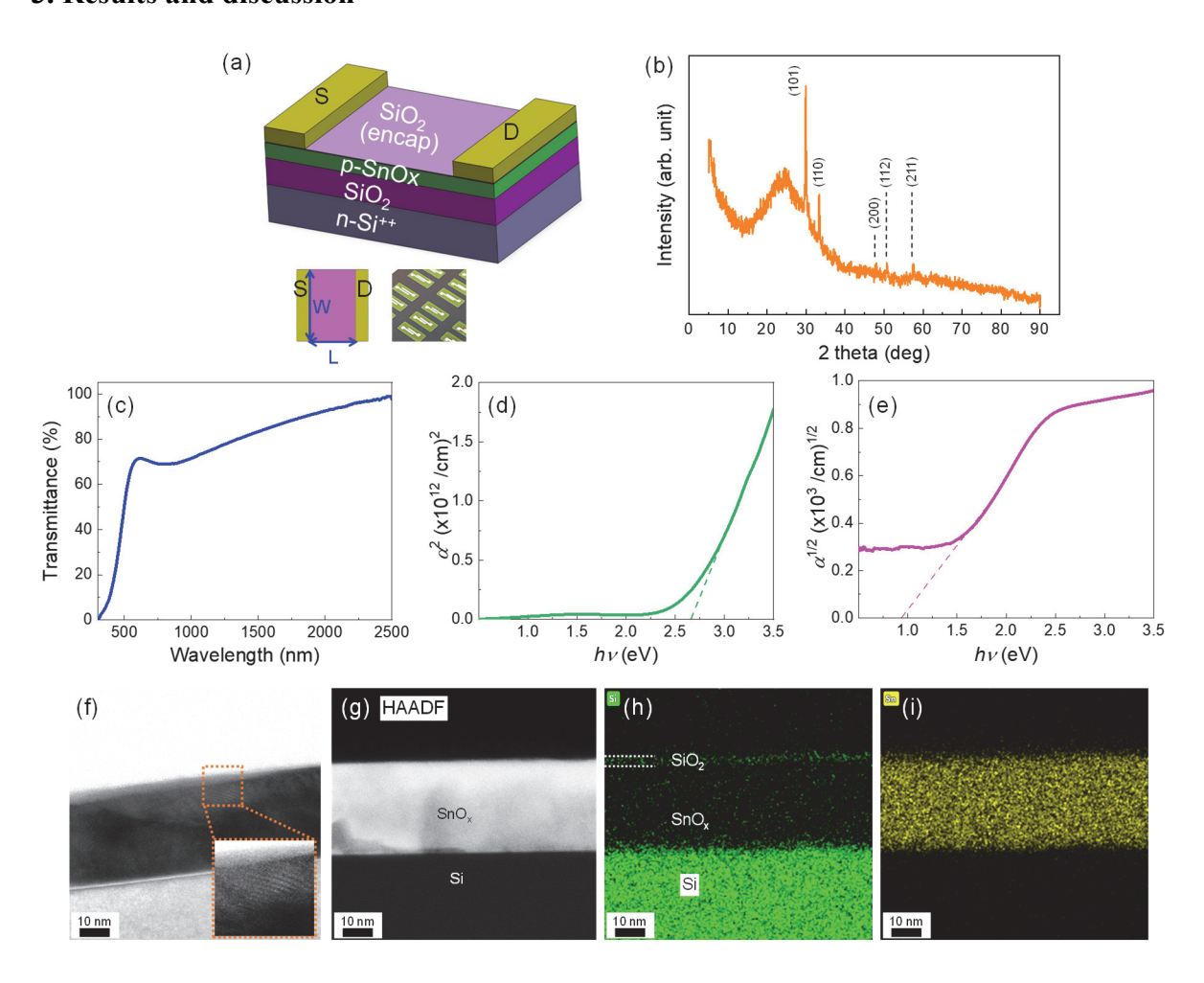


Figure 1. p-SnO_x characteristics and TFT application. (a) schematic and photograph of a TFT device (W/L=1000/100 μ m) fabricated in this study; (b) x-ray diffractogram of poly-crystalline p-SnO_x; UV-Vis-NIR spectra of (c) transmittance at wavelengths ranging 300-2500 nm, Tauc plots of (d) α^2 -hv for direct transition, from which the direct E_g is extracted to be 2.71 eV and (e) $\alpha^{1/2}$ -hv for the indirect transition by which the indirect E_g is estimated to be 0.88 eV; (f) bright field cross-sectional TEM image of a bilayer of SiO₂/p-SnO_x on Si with an inset extended image (orange box), (g) HAADF (dark field) TEM microstructure, (h) EDS mapping image of Si, evidencing a capping layer of SiO₂, and (i) EDS mapping image of Sn.

Bottom-gated TFT devices were fabricated with p-SnO_x as channel and a schematic of the TFT structure is shown in Figure 1(a) with a photograph of the fabricated devices. A typical x-ray diffractogram shown in Figure 1(b) exhibits a polycrystalline state of the resulting p-SnO_x with strong crystallographic intensity from (101) and (110) orientations at diffraction angle, 2θ=29.88° and 33.36°, respectively (JCPDS #06-0395). Other minor peaks are also detected from (200), (112), and (211) planes at $2\theta = 47.91^{\circ}$, 50.74° , and 57.53° , respectively. Optoelectronic properties were measured at wavelengths ranging 300-2500 nm by UV-Vis-NIR spectroscopy, and the results are shown in Figure 1(c-e). The optical transmittance in Figure 1(c) is over 70 % (76% at 550 nm) in the visible regime and increases in the near infrared regime (800-2500 nm). The optical bandgap (E_g) for direct transition was extracted to be ~2.71 eV by extrapolation with a Tauc plot of (absorption coefficient, α)² vs photon energy (hv) in Figure 1(d). The direct E_g value is aligned with those (2.6-3.1 eV) available in the literature ^{6, 47-52}. The indirect bandgap was also determined to be ~0.88 eV from a Tauc plot for the indirect transition of $(\alpha)^{1/2}$ vs hv, which is matched with the values ($\sim 0.7-1.0 \text{ eV}$) found from previous studies, of which the indirect E_g values were estimated from absorption spectra and theoretical calculations^{8, 47, 52, 53}. Cross-sectional microstructures and elemental distributions were investigated through TEM and EDS. Figure 1(d) shows a cross-sectional TEM image of a bilayer of SiO₂/p-SnO_x mimicking the encapsulated channel for the TFT application. In the inset extended TEM image (orange box),

regions of alternating bright and dark contrast/contours indicate a similarly oriented crystalline region of polycrystalline material. At the top of the inset image, a light gray region is also visible without any crystalline features, which is attributed to the encapsulation SiO₂ in the amorphous state. A high-angle annular dark-field (HAADF) TEM image (Fig. 1e) and its associated EDS elemental mapping (Fig. 1f, g) were obtained from a SiO₂/p-SnO_x sample. Figure 1(f) shows an EDS mapping image of Si (green), which clearly showcases the presence of encapsulation SiO₂ on top of SnO_x. The elemental mapping of Sn (yellow) is displayed in Figure 1(g), which is well concentrated in the channel p-SnO_x.

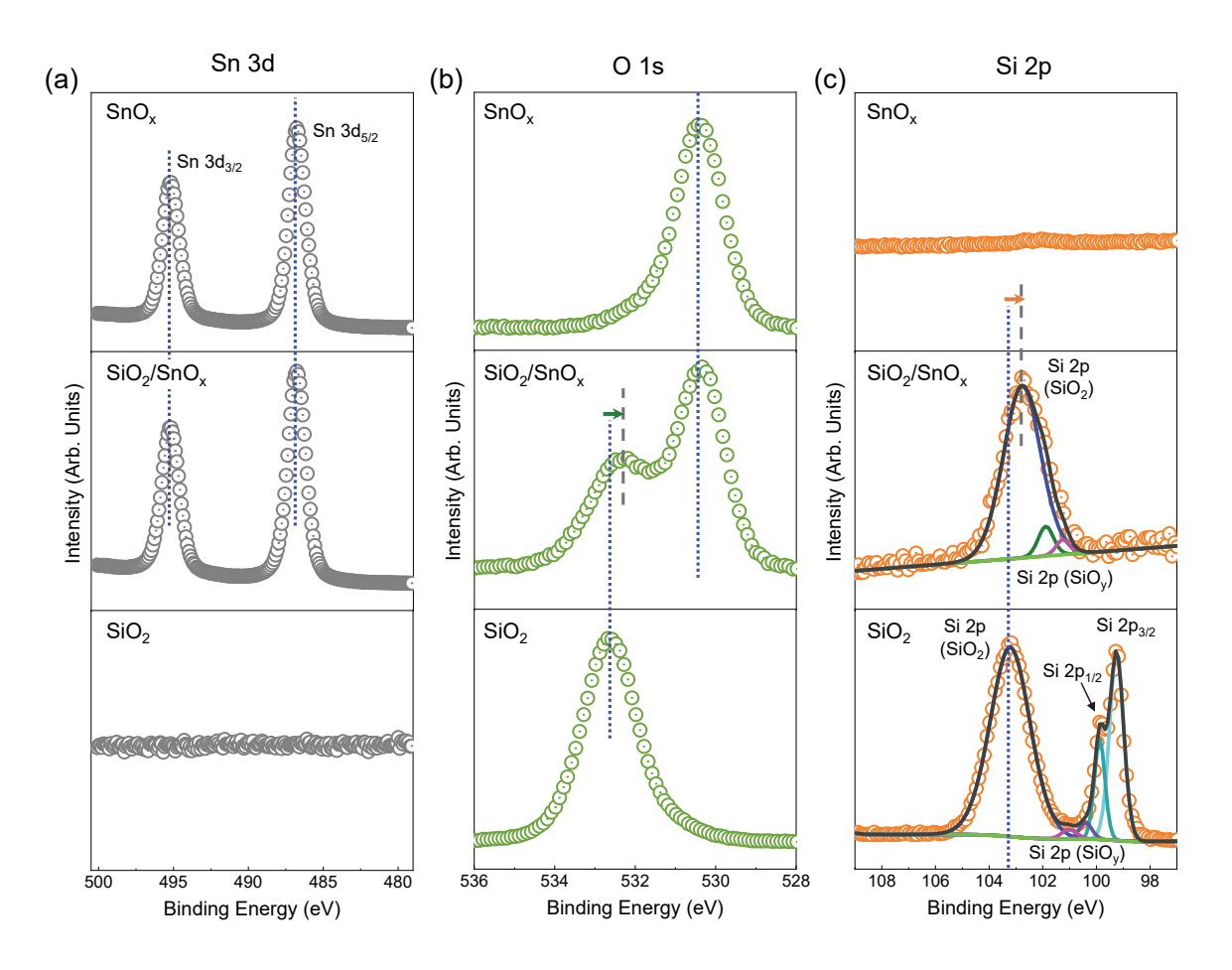


Figure 2. HR XPS investigations of pristine p-SnO_x, encapsulation SiO₂, and bilayer of SiO₂/p-SnO_x for (a) Sn 3d, (b) O 1s, and (c) Si 2p

In order to investigate the effect of the thin SiO₂ layer on the chemical environments of the channel, XPS investigations were conducted on the samples deposited on Si substrate: single layers of SnO_x and SiO₂ and a bi-layer of the SiO₂-encapsulated SnO_x. Since XPS is a surface sensitive analytic technique that detects the binding energy information of the specimen elements from the uppermost 10-15 nm, the chemical information of bi-layer samples, consisting of a thin top coat (3-4 nm SiO₂) as well as an underlying material (i.e., SnO_x in this study), is able to be investigated. Survey scans of the bi-layer samples (in Figure S1, Supporting Information) are shown to include the major elements of Sn, Si, and O, further evidencing the presence of SiO₂ on SnO_x films, while the control samples (single layers) of SnO_x and SiO₂ only display their own elements of (Sn and O) and (Si and O), respectively. Detailed valence states and chemical environments of the major elements are elaborately analyzed through high resolution (HR) XPS measurements. Figure 2(a) shows HR Sn 3d XPS spectra of single layers of SiO₂ and SnO_x, and a bilayer of SiO₂/SnO_x. It should be noted that the detected Sn binding energies from the single layer SnO_x and the bilayer SiO₂/SnO_x are nearly identical for the Sn 3d spin-orbit split pair at 486.79 eV of Sn 3d_{5/2} and 495.12 eV of Sn 3d_{3/2}, respectively. The identical binding energies indicate that the chemical environments of Sn in the SiO₂/p-SnO_x were maintained, relating that no reactions involving Sn occurred during the capping of SiO₂. Note that each Sn 3d spin-orbit component (i.e., 3/2 and 5/2) is symmetric and displays a single peak, which confirms no metallic Sn is present in the resulting p-SnO_x since SnO_x with mixed metallic Sn exhibits two peaks per split where metallic contribution locates at lower binding energies⁶. No significant Sn 3d intensity is observed in the single layer of SiO₂, as expected.

In the HR O 1s XPS spectra in Figure 2(b), the single layers of SiO₂ and p-SnO_x exhibit a nearly symmetric single O 1s peak at 532.5 eV for SiO₂ and ~531 eV for p-SnO_x, respectively. The bilayer SiO₂/p-SnO_x evidently displays the two O 1s peaks due to each contribution from SiO₂ and p-SnO_x. Notice should be taken that in the bilayer of SiO₂/SnO_x, the O 1s peak due to SnO_x is located at the same BE as the single SnO_x; however, the O 1s peak originated from SiO₂ is discernibly shifted to a lower BE (i.e., towards the SnO_x oxygen state) in the SiO₂/SnO_x structure as much as 0.35 eV. The oxygen state shift in SiO₂/SnO_x indicates that oxygen in SiO₂ of the bilayer partially bonded/reacted with SnO_x, possibly near the interface to form chemo-physical bonding between SiO₂ and p-SnO_x.

Figure 2(c) compares HR Si 2p XPS spectra. As expected, no Si 2p information was detected from the single layer of p-SnO_x in the top curve. The single layer SiO₂ spectrum (thickness of 3-4 nm; bottom curve) displays a symmetric peak at BE of 103.23 eV, originating from SiO₂ as well as two distinct spin-orbit components of Si 2p_{1/2} and Si 2p_{3/2} at BE of 99.88 and 99.25 eV, respectively, of which the split is attributed to the substrate Si (single crystalline). In the single layer SiO₂ film, other silicon oxide phases are also observed st-56 near the substrate Si peaks, which indicates that the resulting sputtered SiO₂ is slightly non-stoichiometric.

The bilayer film of SiO₂/p-SnO_x demonstrates an asymmetric SiO₂ peak at BE of 102.86 eV, which is lower as much as 0.37 eV than that of the single layer SiO₂. The observed SiO₂ peak shift/asymmetry and the other non-stoichiometric phases indicate that chemo-physical bonding was made at the interface between the top encapsulation SiO₂ and the underlying p-SnO_x as similarly observed in the HR O 1s XPS investigations of SiO₂/SnO_x. The bonding at the SiO₂ and SnO_x interface, consequently, increased the amount of other silicon oxide phases detected at

BE of \sim 101-102 eV in the SiO₂/p-SnO_x bilayer XPS curve. Note that although the resulting SiO₂ is slightly non-stoichiometric, the encapsulated silicon oxide layer is denoted as SiO₂, otherwise specified when precise stoichiometry information is needed.

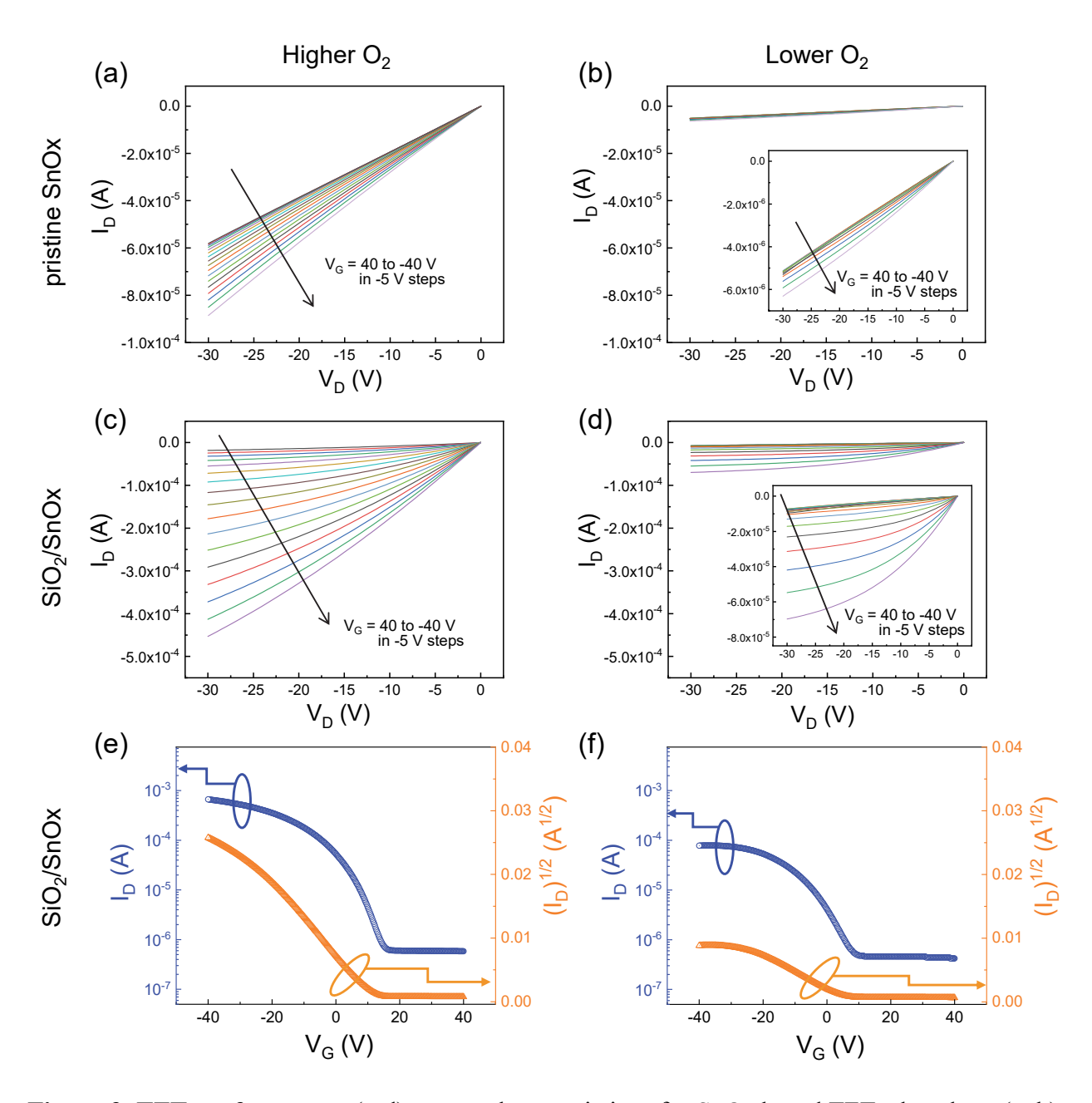


Figure 3. **TFT performance.** (a-d) output characteristics of p-SnO_x-based TFTs that show (a, b) pristine p-SnO_x devices where p-SnO_x was processed at (a) higher O₂ volume potential of 14% and (b) lower potential of 10%; (c, d) encapsulated p-SnO_x TFTs at (c) 14% and (d) 10% O₂ potential, respectively. The encapsulated TFTs present enhanced channel modulation, low off-

state current, and higher on-current, compared to those of pristine counterparts; and (e, f) transfer characteristics of the encapsulated TFTs where the p-SnO_x channel prepared at (e) 14% O₂ and (f) 10% O₂.

P-type oxide TFTs based on p-SnO_x were fabricated in a bottom-gated configuration, as shown earlier in Figure 1(a). In order to investigate and compare the effect of encapsulation of the back channel as well as the oxygen potential in the sputter gas on the TFT behavior, a set of p-SnO_xbased TFTs were prepared. The measured output characteristics are shown in Figure 3. TFTs with pristine SnO_x were compared in Figure 3(a) and (b) where the same y-axis (I_D) scale was used in both plots so that the effect of oxygen volume potential during the sputtering process on the p-type conduction and the TFT performance can be distinctively identified. The resulting transistors operate as depletion mode p-channel field effect devices. The output characteristic curves of the TFT with pristine p-SnO_x deposited at 14% O₂ (i.e., sputter gas volume ratio, O₂/Ar=14/86, resulting in SnO_{1.15} in Fig. S2 in the Supporting Information) show much higher drain currents than those with p-SnO_x prepared at 10% O₂ (yielding SnO_{1.07} in Fig. S2 of HR XPS analyses) in response to the same range of gate bias application (i.e., -40 V \leq V_G \leq 40 V). This trend observed with the pristine p-SnO_x will be compared with those with encapsulated TFTs and related to the doping mechanism in p-SnO_x later in more detail. It should be noted that no strong modulation in channel conduction with high off-state current and weak saturation behavior was observed in the output characteristics of both pristine p-SnO_x TFTs (Fig. 3 a, b), which is attributed to the high carrier density of the resulting p-SnO_x within the processing sputter conditions⁶. Due to the well-known narrow processing window of p-SnO_x, no p-type conduction behavior was observed in SnO_x that was deposited outside of the range (i.e., O₂ volume potential of 10-14%), which leads to the difficulty in further controlling the carrier density of this material (or channel conductance).

The TFT output performance of the encapsulated devices is exhibited in Figure 3(c) and (d). As observed in the pristine p-SnO_x TFTs, higher drain currents were obtained, at the same bias applications, with the channel p-SnO_x that was deposited at higher O₂ potential during depositions. In comparisons of the encapsulated TFTs with the pristine p-SnO_x TFTs, two discernable changes are identified from the output curves of the encapsulated TFTs in Figure 3(c) and (d). First, enhanced channel modulation with low off-state currents was exhibited in both SiO₂-encapsulated TFTs, compared to the pristine counterparts. Since all other components are identical except for the encapsulation SiO₂, it is reasonable to deduce that the SiO₂ covering the back channel contributes to the low off-state current by controlling the injected and arrived carriers from the source and to the drain⁴⁵. The second feature to notice from the output characteristics is the effect of the SiO₂ capping on the doping of p-SnO_x. In the comparison of the TFT performance with and without the SiO₂ capping layer, the drain current of the SiO₂passivated devices increases about an order of magnitude for both O₂ potentials. It is reasonably hypothesized that additional agents (further discussed later with ToF-SIMS and DFT investigations) are doped into the channel p-SnO_x and work as acceptors that additionally generate positively charged free carriers (i.e., holes) in the channel, particularly at the higher gate biases.

Figure 3(e, f) shows device transfer characteristics of the encapsulated TFTs based on p-SnO_x fabricated with 14% and 10% O₂, respectively, where plots of I_D-V_G (blue) are presented on the left y-axis and curves of (I_D)^{1/2}-V_G (orange) are presented on the right y-axis. The drain current on/off ratio is found from the I_D-V_G plots to be >10³ and >10² for the TFTs with 14% and 10%

 O_2 p-SnO_x channel, respectively. The field effect mobility (μ_{FE}) and threshold voltage (V_T) of the TFTs are determined from the slope and the x-axis intercept of the linear extrapolation of the (I_D)^{1/2}-V_G plots according to the equation:

$$I_D = \mu_{FE} C_{ox} \frac{W}{2L} (V_G - V_T)^2$$
 (3)

where the drain current is related to μ_{FE} , V_G , V_T , oxide capacitance (C_{ox}) , and the device aspect ratio of channel width (W) to length (L). The field effect mobility is extracted to be 3.41 and 0.92 cm²/Vs from the TFTs with 14% and 10% O₂ p-SnO_x, respectively, and the threshold voltage is found as 11.1 and 6.1 V, individually. The obtained field effect mobility (3.41 cm²/Vs) is comparable (or slightly higher) to those reported in the literature^{39, 57, 58}. Meanwhile, the transfer performance of the pristine counterparts does not show a switching behavior due to the much inferior channel modulation behavior (Fig. S4 in the Supporting Information). The TFT performance parameters of the pristine and encapsulated p-SnOx TFTs are summarized in Table 1. In our bottom gate TFT configuration, thermally-grown SiO₂ on heavily-doped Si was used as the gate dielectric and p-type SnO_x was directly prepared on the SiO₂/Si structure. Typically, trap states in the dielectric or at the channel/dielectric interface are the main origins of TFT hysteresis. In the present study, comparing the effect of thin encapsulation on the p-SnO_x TFT performance, the identical SiO₂/Si structure was used for the pristine and encapsulated TFTs and the devices were fabricated in parallel at the same batch except only for the encapsulation layer. Therefore, no significant differences in trap-related hysteresis are expected between the pristine and encapsulated TFTs. Despite the similar trap states expected in the dielectric or at the channel/dielectric interface, hysteresis may appear in the two devices (i.e., pristine and encapsulated) due to the high gate biases (V_G from -40 V to 40 V). In order to investigate the origin of the enhanced TFT performance and doping mechanisms, elemental distribution analysis was conducted across the thickness of the pristine channel p-SnO_x and SiO₂/p-SnO_x using ToF-SIMS which will be discussed later in Figure 4.

In the literature, TFT devices employing p-SnO_x have been fabricated using various techniques including sputtering (both dc and rf) ^{15, 59}, pulsed laser deposition ³⁹, atomic layer deposition ⁶⁰, evaporation ⁶¹, and liquid-phase processing ⁶². These processes typically require elevated temperatures during the fabrication or post-process annealing, ranging temperatures from 150 to 550 °C, to control the crystalline phase of resulting p-SnO_x or to achieve p-type conductivity. Regardless of the process techniques, the mobility and on/off current ratio of p-SnO_x TFTs are inferior, as low as $\sim 0.01-3$ cm²/Vs and 10^2-10^4 ^{27, 29, 39, 62}, respectively, compared to $\sim 10-20$ cm²/Vs and 10⁵-10⁷ of typical n-type counterparts such as InZnO and InGaZnO ^{2, 45, 63, 64} for TFT channel applications. The typical low carrier mobility of p-SnO_x is attributed to the localized oxygen 2p orbitals near the valence band ^{8, 29, 65}. Zhong et al. achieved relatively high field effect mobility (6.5 cm²/Vs) and high switching ratio (10⁵) of p-SnO_x TFTs through dual-gate TFT structures where the enhanced performance is attributed to the coupled top/bottom gate biases which enabled more efficient channel modulation ⁵⁹. Barros *et al.* achieved a high field effect mobility of 4.6 cm²/Vs and an on/off ratio of ~10⁵ through composition engineering of roomtemperature processed p-SnO_x and low-temperature annealing at 200 °C ¹⁵. Nomura et al. leveraged hydrogen environment annealing to passivate oxygen vacancy defects in p-SnO_x and hence enhance TFT device performance with a high switching ratio of 10⁵ ³⁹.

Table 1. p-type SnOx-based TFT performance, comparing pristine and encapsulated devices

p-type TFTs	P _{O2} in the sputter gas (%)	Operation mode	$\mu_{\mathrm{FE}} \ (\mathrm{cm^2/Vs})$	On/off ratio	$V_{T}(V)$
Pristine	10	Depletion	0.003	~2	>40
	14		0.18	~2	>40
Encapsulated	10	Depletion	0.92	10^{2}	6.1

14 3.41 10^3 11.1

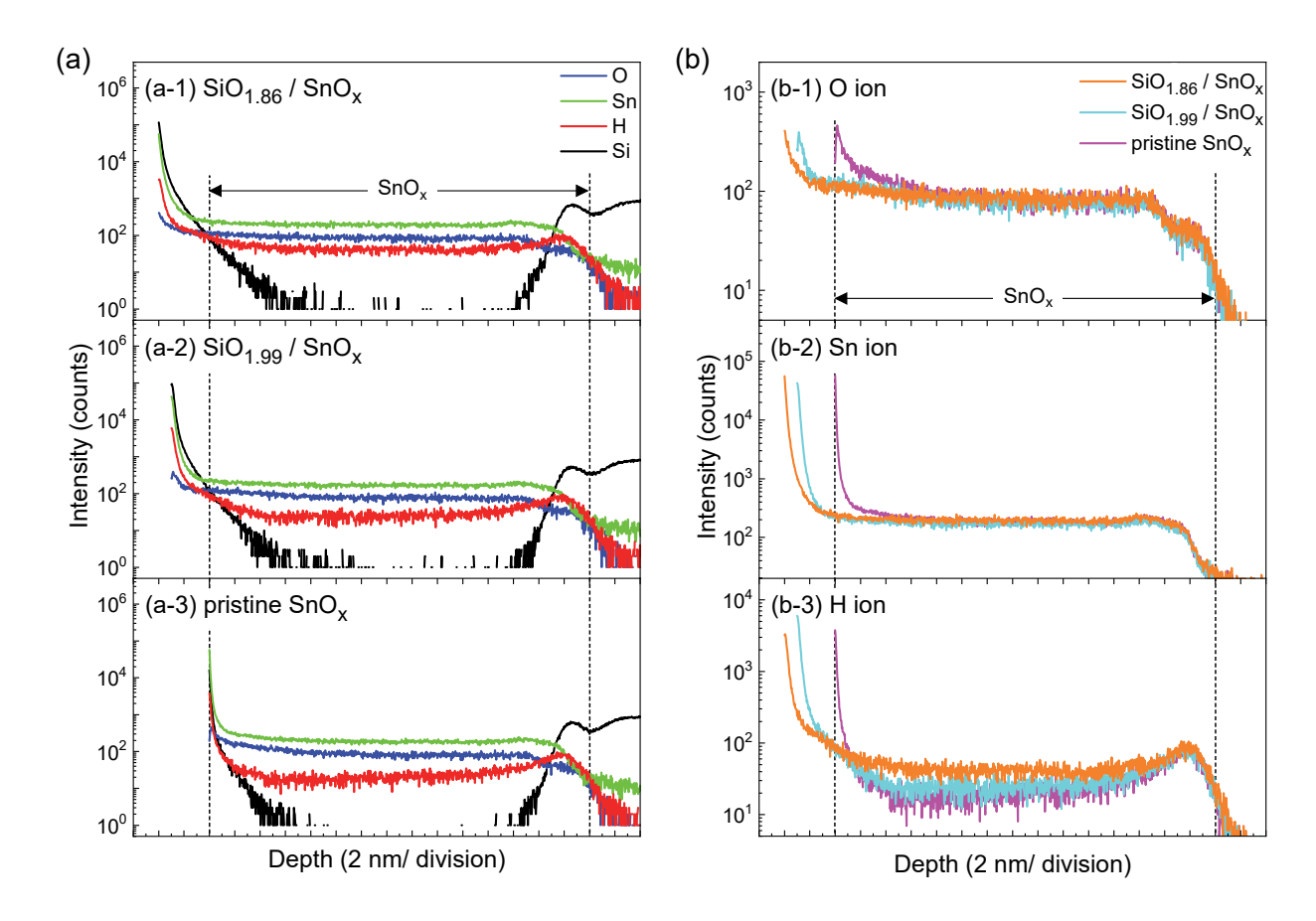


Figure 4. ToF-SIMS depth profiling of the major element and additional H ion of the SiO₂/SnO_x and pristine SnO_x films as a function of (a) sample structure and (b) ion

ToF-SIMS depth profiling results in **Figure 4** show the distribution of the major ions of the pristine p-SnO_x and SiO₂/p-SnO_x specimens. In addition to the major ions, hydrogen ion was also tracked to identify its presence and the effect on the chemical and electrical properties of the p-SnO_x and the TFT performance. In order to compare the hydrogen permeation mechanism, an additional SiO₂/SnO_x sample was included in the SIMS analysis, where the SiO₂ layer was grown at a higher O₂-contained sputter gas (O₂/Ar=5/95; resulting in SiO_{1.99}), compared to that

deposited at pure Ar conditions (resulting in SiO_{1.86}). The stoichiometry of SiO_y was determined from HR XPS element area analyses in Figure S3 (Supporting Information), from which the SiO_{1.99} is considered a pseudo-stoichiometric phase (SiO_{1.99}≈SiO₂) and the SiO_{1.86} is regarded as an oxygen deficient counterpart. In addition to the TEM/EDS images in Figure 1, it is further verified that a thin layer of SiO₂ (~3-4 nm thick) is well present on p-SnO_x (Fig. 4(a-1) and (a-2); (b-1) and (b-2)), in comparison with the pristine layer of p-SnO_x in Fig. 4(a-3) and (b-3). The major composition ions of Sn and O are confirmed to be dominantly present over the 30 nm thick p-SnO_x layer in all three specimens. It should also be noted that non-negligible H ion intensity is clearly detected in the entire thickness of p-SnO_x in all the samples.

In order for direct comparisons of the ion distribution, the ToF-SIMS results in Figure 4(a) were rearranged as a function of ion element, of which the plots are shown in Figure 4(b). The O ion distribution, showcased in Figure 4(b-1), is noticed that the O ion concentration of pristine SnO_x near the surface (i.e., back channel in bottom-gated TFTs) is higher than that of the bulk regime and that of the SiO₂-encapsulated p-SnO_x. The demonstrated O ion difference between the pristine and encapsulated samples indicates that the pristine p-SnO_x surface adsorbed oxygen from the air while the encapsulation SiO₂ effectively suppresses the oxygen adsorption on the surface of p-SnO_x due to the limited diffusion of oxygen in SiO₂.⁶⁶⁻⁶⁹ This observed O diffusion barrier performance of SiO₂ is supported by several studies available in the literature. Fahlteich *et al.*⁶⁶ reported that the oxygen permeation rate in sputter-processed SiO₂ is as low as 0.14 cm³/m²d bar, comparable to or lower than those of Al₂O₃ and TiO₂ (0.1 and 0.38 cm³/m²d bar, respectively). Wertheimer *et al.*⁶⁷ and von Rohr *et al.*^{68, 69} also reported the effective oxygen and water barrier performance of SiO₂ processed through plasma-enhanced chemical-vapor-

deposition (known as PECVD) where the authors identified that the barrier performance depends on the defect concentrations and microstructures. Similar results were also achieved by a nonvacuum processed SiO₂ through atmospheric pressure plasma jet deposition⁷⁰. No discernible differences in the O ion distribution are detected between the two encapsulated cases. Since the surface adsorbed oxygen is known to cause performance variation of oxides and generate trap sites, the demonstrated oxygen barrier capability is to exclude the potential performance issues regarding oxygen adsorption^{71, 72}. For Sn ion distributions shown in Figure 4(b-2), no significant changes were observed across the channel p-SnO_x for all three samples. An H ion distribution by ToF-SIMS is presented in Figure 4(b-3) where the noticeably highest H ion intensity is observed throughout the SnO_x region of the more O-deficient encapsulation sample (i.e., SiO_{1.86}/SnO_x), compared to the other two samples. In the SiO_{1.99}/SnO_x specimen, the H ion intensity is slightly higher than that of the pristine p-SnO_x film. The results indicate that (i) SiO₂ selectively permeates hydrogen, and (ii) the permeability varies with the O/Si stoichiometry in the layer which can be tuned by growth conditions (i.e., oxygen fraction in the sputter gas). From the SIMS results, it is identified that the less oxygen stoichiometry may lead to the higher hydrogen accommodation capability than that of higher stoichiometry in silicon oxides, and (iii) the presence of H and its concentration differences in p-SnO_x may be related to the channel carrier density in consideration of the enhanced on-current of the TFTs shown in Figure 3. The selective hydrogen permeation through SiO₂, while blocking other species, has been widely considered in the field of electrochemistry such as H⁺ conducting membranes in intermediatetemperature fuel cells⁷³⁻⁷⁵. Jo et al. ⁷³ recently reported an electrochemistry study with cyclic voltammetry (CV) and electrochemical impedance spectroscopy where an ultra-thin amorphous SiO₂ layer is identified to selectively transfer H⁺ across the interface between layers, while the

permeation of oxygen is effectively blocked. Similar results were reported by Lee et al. 76 where a selective transport of H⁺ was proved using CV measurements from a heavily-doped Si/SiO₂/electrolyte system. It should be noted that they also reported that the formed and transported H⁺ serves as a reducing media by accepting electrons from the hosting matrix, particularly in the presence of bias applications. Lee et al. 76 uniquely exploited the reducing capability of the Si/SiO₂/electrolyte system with hydrogen ions for electrochemical reduction of CO₂ and O₂ and electrochemical syntheses of bimetallic nanocrystals under electrical biases⁷⁶. Further studies on the selective hydrogen permeation of SiO₂ have been reported, where the generation and permeation of hydrogen are found to be facilitated in the presence of biases practically greater than approximately 2 V in the presence of H₂O ^{77, 78}. In the encapsulated devices, large biases (up to ± 40 V) were applied to the gate electrode with respect to the source electrode where the electrodes were placed in the same ambient conditions and, therefore, the permeation may be generated on the encapsulation surface (i.e., SiO₂) or at the source/encapsulation interface 73, 77-79. This selective H⁺ transfer through SiO₂ and bias-assisted reduction capability concur with the TFT performance observed in this study. The permeated H⁺ in the channel p-SnO_x, of which the presence is evidenced in Figure 4(b-3) through SIMS, is likely to be activated to serve as acceptor by the application of gate biases and hence increase the channel carrier density and the drain current. The role of SiO₂ encapsulation on top of p-SnO_x is schematically compared with that without encapsulation in Fig. S4 (Supporting Information).

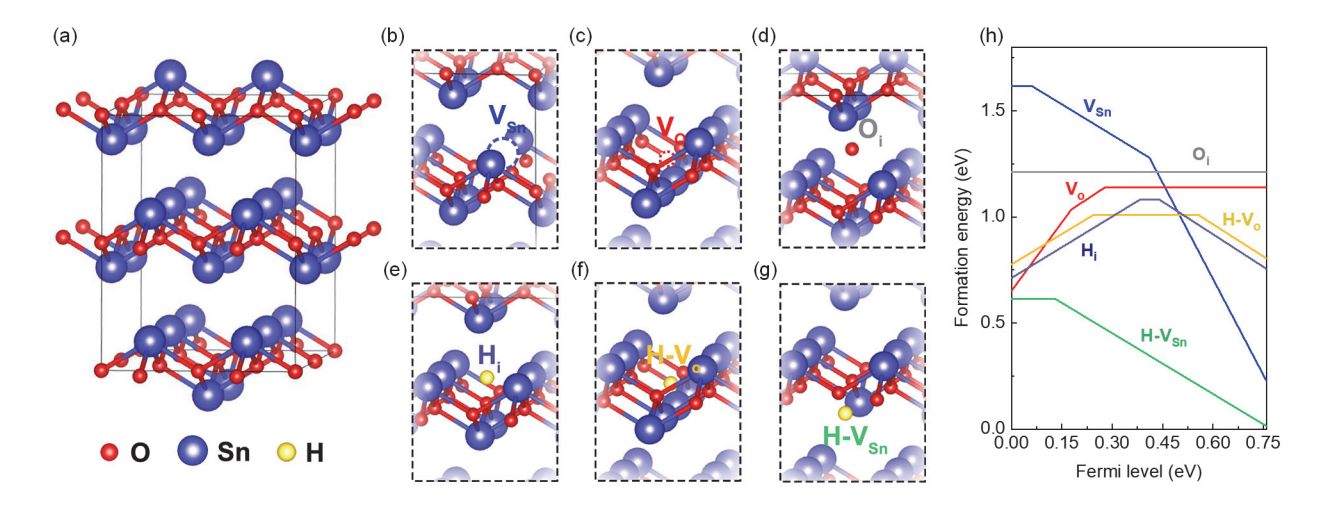


Figure 5. DFT calculation of impurities in p-type SnO. (a) Crystal structure of SnO; (b-g) Crystal structures with possible defects of (b) Vsn, (c) Vo, (d) Oi, (e) Hi, (f) H-Vo, and (g) H-Vsn; and (h) Formation energies of possible defects in SnO as a function of Fermi level.

To further validate the H-related doping mechanism in p-SnO_x, DFT calculations were conducted. The defect formation energy of various defects was calculated to identify the defects favored in SnO and their contribution to p-type doping. The formation energy of a defect in SnO is given by:

(4)

 $\triangle E_f(defect,q) = E_T(defect,q) - E_T(perfect,q) + \mu_{Sn} + \mu_O + q\varepsilon_F$

where
$$E_T(defect, q)$$
 is the total energy of a supercell with a defect in a charge state q and $E_T(perfect, q)$ is the total energy of a perfect supercell in a charge state q . μ_{Sn} and μ_O are the atomic chemical potentials of Sn and O, respectively. ε_F is the electron chemical potential and measured from the valence-band maximum (VBM), which is set to 0 eV. The crystal structure of perfect SnO as demonstrated in Fig. 5(a) and the crystal lattice structure of the defects considered are exhibited in Fig. 5(b-g): (b) Vsn, (c) Vo, (d) Oi, (e) Hi, (f) H-Vo, and (g) H-Vsn. The Sn vacancy, Vsn has a (0/-) transition level at 0.06 eV and (-/2-) at 0.41 eV above VBM as indicated in Fig. 5(b) and (h). Those of Vo from +2 to +1 and +1 to 0 are located at 0.18 eV and 0.28 eV, respectively. Oi shows no defect transition level in the calculated band gap shown in Fig. 5(h),

implying the existence of O interstitials may not work as a p-type dopant. Hydrogen-related defects were considered to include H interstitial and interactions between hydrogen and two kinds of vacancies (i.e.: V_{Sn} and V_O), which are marked as H_i, H-V_O, and H-V_{Sn} in the defect formation energy diagram (Fig. 5e, f, g, respectively). Hi plays a role as amphoteric defects in SnO with the $(\pm/0)$ and (0/-) transition level at 0.38 eV and 0.42 eV in our DFT calculation 30,39 , ^{40, 42, 80}. The H_i formation energy plot indicates that H_i can be either p-type or n-type dopants, given the locations of these defect energy levels within the bandgap. However, in the diagram, the H_i states are identified to take deep-level donor or deep-level acceptor, and therefore neither of them works as active dopants in SnO for both polarities. For the H-Vo configuration structure in Fig. 5(f), hydrogen occupies the center position of the oxygen vacancy and forms a substitutional impurity H-V₀. The H-V₀ was calculated to work as an amphoteric defect with the (0/+) and (-/0) transition levels located at 0.24 eV and 0.55 eV, respectively. Similar to the H₁ case above, H-Vo does not contribute as active dopants to either polarity conduction. The complex impurity structure of H-V_{Sn} sits at the center of the V_{Sn} as shown in the lattice structure, Fig. 5g and the transition level of H-V_{Sn} from -1 to 0 (i.e., possible acceptor) was located at 0.13 eV above VBM in Fig. 5(g). Among all these impurities in SnO, the H-V_{Sn} has the lowest formation energy, which suggests the source of the p-type conductivity in SnO (i.e., shallow acceptor) in the presence of hydrogen. These DFT calculations support the role of hydrogen on the p-type doping in SnO_x where the defect cluster of H-V_{Sn} may account for the enhanced doping concentration as extrinsic p-dopant.

The role of hydrogen in p-type SnO is not clearly understood yet and is controversial in the literature. Nomura *et al.* found that hydrogenating SnO by thermal annealing in hydrogen

ambient was able to reduce subgap defect states at annealing temperatures up to 400 °C, where the reduced subgap states were validated through reduced absorption, enhanced TFT transfer performance with low-off current, and density-of-state calculations³⁹. The mobility of this hydrogenated p-type SnO was achieved as high as ~2 cm²/Vs.³⁹ Varley et al. predicted a possible hydrogen doping mechanism in p-type SnO from first-principles calculations, in which the doped hydrogen forms shallow-level acceptors by generating complex impurities (such as H atom located at the center of the oxygen vacancy, H-V₀ or tin vacancy, H-V_{sn}) other than the singlespecie defects. They also suggested that the interstitial H, which is a single-specie defect, acts as an amphoteric impurity in SnO ³⁰. However, Becker et al. reported lattice parameters investigations that hydrogen in p-type SnO takes interstitial sites (i.e., H_i) and works as active acceptors rather than complex impurities³⁷. Later, Yim reported a DFT calculation study, in which the authors claim that the doping of p-type SnO was induced by hydrogen complex impurities while interstitial H acts as only a donor ⁴². Yim's report is further supported by Xue et al. who reported that hydrogen complex impurities allow for doping of p-type SnO, rather than H_i, acting as an amphoteric impurity⁴⁰. Although the role of hydrogen in p-type doping in SnO is not fully established, these quite a few reports concerning the hydrogen impurity complexes as a favorable acceptor agree with our DFT analysis and support our discussion on the selective hydrogen permeation through a thin SiO₂ layer and its effect on the TFT performance. ^{30, 40, 42}

4. Conclusion

This study suggests facile strategies to achieve high performance TFTs with p-type SnO_x through a thin encapsulation layer that adjusts channel carrier injection and selectively permeates hydrogen while blocking oxygen. The inclusion of a thin SiO₂ film (3-4 nm) effectively reduces

the device off-state current without sacrificing the on-state current. The effect of SiO₂

encapsulation on the extrinsic doping of p-SnO_x and the TFT performance is explored through a

series of investigations of XPS, ToF-SIMS, and DFT calculations, by which the presence of

hydrogen across the entire p-SnO_x channel is identified and an impurity complex of H-V_{Sn} in the

lattice is found to be the favorable dopant in p-SnO_x. The oxygen stoichiometry in the

encapsulation layer is likely to be a governing factor of the hydrogen permeability and hence the

extrinsic doping capability. The resulting encapsulated p-SnO_x TFTs demonstrate superior

performance stability in ambient air at room temperature and elevated temperatures (up to

300 °C evaluated in this study) with high field effect mobility of 3.41 cm²/Vs, drain current

on/off ratio of 10³, and threshold voltages of ~5-10 V. These findings may be of significant

relevance to p-SnO_x TFT studies that show issues of tuning channel carrier density and

consequent conduction modulation (either too high or too low), and reliability due to oxygen

adsorption on the channel surface.

AUTHOR INFORMATION

Corresponding Author

*Sunghwan Lee. Email: sunghlee@purdue.edu

Author Contributions

S.L. conceived the study. D.L. and H.P. prepared the materials and fabricated the devices. S.C.,

H.P., J.P., C.S.K., N.K. and H.W.S. conducted material characterizations. Y.Z. performed DFT

calculations. D.L. and Y.Z. performed the device characterization. S.L., Hongsik P., J.B., Y.Z.

and D.L. analyzed the data and wrote the manuscript.

28

Notes

The authors declare no competing financial interest.

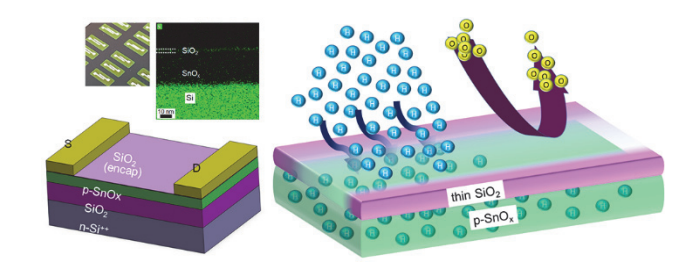
Supporting Information

XPS survey scans; XPS HR scans for O 1s, Sn 3d, and Si 2p; Transfer characteristics of pristine p-SnO_x TFTs; Schematic representations of the role of SiO₂ encapsulation; Annealing of p-SnO_x in a hydrogen atmosphere

Acknowledgments

This work was supported by the U.S. National Science Foundation (NSF) Award No. ECCS-1931088. S.L. and H.W.S. acknowledge the support from the Improvement of Measurement Standards and Technology for Mechanical Metrology (Grant No. 21011042) by KRISS. K.N. was supported by Basic Science Research Program through the National Research Foundation (NRF) Korea (2021R11A1A01051246) funded by the Ministry of Education. H.P. acknowledges the support from NRF Korea (2020R1A4A1019518) funded by the Ministry of Science and ICT (MSIT), Korea.

Table of Contents (TOC)



References

- 1. Nomura, K.; Ohta, H.; Takagi, A.; Kamiya, T.; Hirano, M.; Hosono, H., Room-temperature fabrication of transparent flexible thin-film transistors using amorphous oxide semiconductors. *Nature* **2004**, *432* (7016), 488-492.
- 2. Barquinha, P.; Martins, R.; Pereira, L.; Fortunato, E., *Transparent Oxide Electronics: From Materials to Devices*. Wiley: 2012.
- 3. Dey, S.; Nag, S.; Santra, S.; Ray, S. K.; Guha, P. K., Voltage-controlled NiO/ZnO p—n heterojunction diode: a new approach towards selective VOC sensing. *Microsystems & Nanoengineering* **2020**, *6* (1), 35.
- 4. Pereira, M. E.; Deuermeier, J.; Freitas, P.; Barquinha, P.; Zhang, W.; Martins, R.; Fortunato, E.; Kiazadeh, A., Tailoring the synaptic properties of a-IGZO memristors for artificial deep neural networks. *APL Materials* **2022**, *10* (1), 011113.
- 5. Qin, F.; Zhang, Y.; Park, H.; Kim, C. S.; Lee, D. H.; Jiang, Z.-T.; Park, J.; No, K.; Park, H.; Song, H. W.; Lee, S., Factors Determining the Resistive Switching Behavior of Transparent InGaZnO-Based Memristors. *physica status solidi (RRL) Rapid Research Letters* **2022**, *16* (7), 2200075.
- 6. Lee, D. H.; Park, H.; Clevenger, M.; Kim, H.; Kim, C. S.; Liu, M.; Kim, G.; Song, H. W.; No, K.; Kim, S. Y.; Ko, D.-K.; Lucietto, A.; Park, H.; Lee, S., High-Performance Oxide-Based p—n Heterojunctions Integrating p-SnOx and n-InGaZnO. *ACS Applied Materials & Interfaces* **2021**, *13* (46), 55676-55686.
- 7. Kawazoe, H.; Yasukawa, M.; Hyodo, H.; Kurita, M.; Yanagi, H.; Hosono, H., P-type electrical conduction in transparent thin films of CuAlO2. *Nature* **1997**, *389* (6654), 939-942.
- 8. Ogo, Y.; Hiramatsu, H.; Nomura, K.; Yanagi, H.; Kamiya, T.; Hirano, M.; Hosono, H., p-channel thin-film transistor using p-type oxide semiconductor, SnO. *Applied Physics Letters* **2008**, *93* (3), 032113.
- 9. De Wit, J. H. W.; Van Unen, G.; Lahey, M., Electron concentration and mobility in In2O3. *J Phys Chem Solids* **1977**, *38* (8), 819-824.
- 10. Fang, G.; Li, D.; Yao, B.-L., Fabrication and vacuum annealing of transparent conductive AZO thin films prepared by DC magnetron sputtering. *Vacuum* **2002**, *68* (4), 363-372.
- 11. Lee, S.; Paine, D. C., Identification of the native defect doping mechanism in amorphous indium zinc oxide thin films studied using ultra high pressure oxidation. *Applied Physics Letters* **2013**, *102* (5), 052101.
- 12. Wahlström, E.; Vestergaard, E. K.; Schaub, R.; Rønnau, A.; Vestergaard, M.; Lægsgaard, E.; Stensgaard, I.; Besenbacher, F., Electron Transfer-Induced Dynamics of Oxygen Molecules on the TiO2(110) Surface. *Science* **2004**, *303* (5657), 511-513.
- 13. Peelaers, H.; Chabinyc, M. L.; Van de Walle, C. G., Controlling n-Type Doping in MoO3. *Chem. Mat.* **2017**, *29* (6), 2563-2567.
- 14. Yabuta, H.; Kaji, N.; Hayashi, R.; Kumomi, H.; Nomura, K.; Kamiya, T.; Hirano, M.; Hosono, H., Sputtering formation of p-type SnO thin-film transistors on glass toward oxide complimentary circuits. *Appl. Phys. Lett.* **2010**, *97* (7).
- 15. Barros, R.; Saji, K. J.; Waerenborgh, J. C.; Barquinha, P.; Pereira, L.; Carlos, E.; Martins, R.; Fortunato, E., Role of Structure and Composition on the Performances of P-Type Tin Oxide Thin-Film Transistors Processed at Low-Temperatures. *Nanomaterials (Basel)* **2019**, *9* (3).
- 16. Hautier, G.; Miglio, A.; Ceder, G.; Rignanese, G.-M.; Gonze, X., Identification and design principles of low hole effective mass p-type transparent conducting oxides. *Nat Commun* **2013**, *4*.
- 17. Yim, K.; Youn, Y.; Lee, M.; Yoo, D.; Lee, J.; Cho, S. H.; Han, S., Computational discovery of p-type transparent oxide semiconductors using hydrogen descriptor. *npj Computational Materials* **2018**, *4* (1), 17.
- 18. Dhananjay; Chu, C.-W.; Ou, C.-W.; Wu, M.-C.; Ho, Z.-Y.; Ho, K.-C.; Lee, S.-W., Complementary inverter circuits based on p-SnO2 and n-In2O3 thin film transistors. *Applied Physics Letters* **2008**, *92* (23).

- 19. Ou, C.-W.; Dhananjay; Ho, Z. Y.; Chuang, Y.-C.; Cheng, S.-S.; Wu, M.-C.; Ho, K.-C.; Chu, C.-W., Anomalous p-channel amorphous oxide transistors based on tin oxide and their complementary circuits. *Applied Physics Letters* **2008**, *92* (12), 122113.
- 20. Fortunato, E.; Barros, R.; Barquinha, P.; Figueiredo, V.; Park, S.-H. K.; Hwang, C.-S.; Martins, R., Transparent p-type SnOx thin film transistors produced by reactive rf magnetron sputtering followed by low temperature annealing. *Applied Physics Letters* **2010**, *97* (5).
- 21. Togo, A.; Oba, F.; Tanaka, I.; Tatsumi, K., First-principles calculations of native defects in tin monoxide. *Physical Review B* **2006**, *74* (19).
- 22. Guo, Y. Q.; Tan, R. Q.; Li, X.; Zhao, J. H.; Luo, Z. L.; Gao, C.; Song, W. J., Shape-controlled growth and single-crystal XRD study of submillimeter-sized single crystals of SnO. *CrystEngComm* **2011**, *13* (19), 5677-5680.
- 23. Eqbal, E.; Anila, E. I., Properties of transparent conducting tin monoxide(SnO) thin films prepared by chemical spray pyrolysis method. *Physica B: Condensed Matter* **2018**, *528*, 60-65.
- 24. Jia, J.; Sugane, T.; Nakamura, S.-i.; Shigesato, Y., p-type conduction mechanism in continuously varied non-stoichimetric SnOx thin films deposited by reactive sputtering with the impedance control. *Journal of Applied Physics* **2020**, *127* (18), 185703.
- 25. Chen, P.-J.; Jeng, H.-T., Phase diagram of the layered oxide SnO: GW and electron-phonon studies. *Scientific Reports* **2015**, *5* (1), 16359.
- 26. Jaśkaniec, S.; Kavanagh, S. R.; Coelho, J.; Ryan, S.; Hobbs, C.; Walsh, A.; Scanlon, D. O.; Nicolosi, V., Solvent engineered synthesis of layered SnO for high-performance anodes. *npj 2D Materials and Applications* **2021**, *5* (1), 27.
- 27. Fortunato, E.; Barros, R.; Barquinha, P.; Figueiredo, V.; Park, S.-H. K.; Hwang, C.-S.; Martins, R., Transparent p-type SnOx thin film transistors produced by reactive rf magnetron sputtering followed by low temperature annealing. *Applied Physics Letters* **2010**, *97* (5), 052105.
- 28. Togo, A.; Oba, F.; Tanaka, I.; Tatsumi, K., First-principles calculations of native defects in tin monoxide. *Physical Review B* **2006**, *74* (19), 195128.
- 29. Yabuta, H.; Kaji, N.; Hayashi, R.; Kumomi, H.; Nomura, K.; Kamiya, T.; Hirano, M.; Hosono, H., Sputtering formation of p-type SnO thin-film transistors on glass toward oxide complimentary circuits. *Applied Physics Letters* **2010**, *97* (7), 072111.
- 30. Varley, J. B.; Schleife, A.; Janotti, A.; Van de Walle, C. G., Ambipolar doping in SnO. *Applied Physics Letters* **2013**, *103* (8), 082118.
- 31. Zhao, J.; Zhao, X. J.; Ni, J. M.; Tao, H. Z., Structural, electrical and optical properties of p-type transparent conducting SnO2:Al film derived from thermal diffusion of Al/SnO2/Al multilayer thin films. *Acta Materialia* **2010**, *58* (19), 6243-6248.
- 32. Lee, C.-H.; Nam, B.-A.; Choi, W.-K.; Lee, J.-K.; Choi, D.-J.; Oh, Y.-J., Mn:SnO2 ceramics as p-type oxide semiconductor. *Materials Letters* **2011**, *65* (4), 722-725.
- 33. Guo, W.; Fu, L.; Zhang, Y.; Zhang, K.; Liang, L. Y.; Liu, Z. M.; Cao, H. T.; Pan, X. Q., Microstructure, optical, and electrical properties of p-type SnO thin films. *Applied Physics Letters* **2010**, *96* (4), 042113.
- 34. Janotti, A.; Van de Walle, C. G., Sources of unintentional conductivity in InN. *Applied Physics Letters* **2008**, *92* (3), 032104.
- 35. Hofmann, D. M.; Hofstaetter, A.; Leiter, F.; Zhou, H.; Henecker, F.; Meyer, B. K.; Orlinskii, S. B.; Schmidt, J.; Baranov, P. G., Hydrogen: A Relevant Shallow Donor in Zinc Oxide. *Physical Review Letters* **2002**, *88* (4), 045504.
- 36. Nomura, K., 39.2: Invited Paper: Recent Progress of Oxide-Semiconductor-Based P-channel TFTs. *SID Symposium Digest of Technical Papers* **2015**, *46* (1), 591-594.

- 37. Becker, M.; Hamann, R.; Hartung, D.; Voget-Grote, C.; Graubner, S.; Hoffmann, P.; Ronning, C.; Polity, A.; Klar, P. J., Controlling the p-type conductivity of SnO by doping with nitrogen and hydrogen. *Journal of Applied Physics* **2019**, *125* (8), 085703.
- 38. Varley, J. B.; Janotti, A.; Singh, A. K.; Van de Walle, C. G., Hydrogen interactions with acceptor impurities in SnO2: First-principles calculations. *Physical Review B* **2009**, *79* (24), 245206.
- 39. Lee, A. W.; Le, D.; Matsuzaki, K.; Nomura, K., Hydrogen-Defect Termination in SnO for p-Channel TFTs. *ACS Applied Electronic Materials* **2020**, *2* (4), 1162-1168.
- 40. Xue, L.; Yang, Z.; Chen, B.; Li, H.; Zhang, J., The first-principles study of nH–VSn complex: impurity effects on p-type SnO monolayer. *Physical Chemistry Chemical Physics* **2020**, *22* (34), 19275-19281.
- 41. Nam, V. H.; Van Viet, P.; Van Hieu, L.; Thi, C. M., First-principles calculations for hydrogenation of acceptor defects in Li-doped SnO2. *Materials Research Express* **2016**, *3* (10), 105901.
- 42. Yim, S.; Kim, T.; Yoo, B.; Xu, H.; Youn, Y.; Han, S.; Jeong, J. K., Lanthanum Doping Enabling High Drain Current Modulation in a p-Type Tin Monoxide Thin-Film Transistor. *ACS Applied Materials & Interfaces* **2019**, *11* (50), 47025-47036.
- 43. Barquinha, P.; Vila, A. M.; Goncalves, G.; Martins, R.; Morante, J. R.; Fortunato, E.; Pereira, L., Gallium-indium-zinc-oxide-based thin-film transistors: Influence of the source/drain material. *IEEE Transactions on Electron Devices* **2008**, *55* (4), 954-960.
- 44. Lee, S.; Song, Y.; Park, H.; Zaslavsky, A.; Paine, D. C., Channel scaling and field-effect mobility extraction in amorphous InZnO thin film transistors. *Solid-State Electronics* **2017**, *135*, 94-99.
- 45. Liu, M.; Kim, H.; Wang, X.; Song, H. W.; No, K.; Lee, S., Carrier Density-Tunable Work Function Buffer at the Channel/Metallization Interface for Amorphous Oxide Thin-Film Transistors. *ACS Applied Electronic Materials* **2021**, *3* (6), 2703-2711.
- 46. Giannozzi, P.; Baroni, S.; Bonini, N.; Calandra, M.; Car, R.; Cavazzoni, C.; Ceresoli, D.; Chiarotti, G. L.; Cococcioni, M.; Dabo, I.; Dal Corso, A.; de Gironcoli, S.; Fabris, S.; Fratesi, G.; Gebauer, R.; Gerstmann, U.; Gougoussis, C.; Kokalj, A.; Lazzeri, M.; Martin-Samos, L.; Marzari, N.; Mauri, F.; Mazzarello, R.; Paolini, S.; Pasquarello, A.; Paulatto, L.; Sbraccia, C.; Scandolo, S.; Sclauzero, G.; Seitsonen, A. P.; Smogunov, A.; Umari, P.; Wentzcovitch, R. M., QUANTUM ESPRESSO: a modular and open-source software project for quantum simulations of materials. *Journal of Physics: Condensed Matter* **2009**, *21* (39), 395502.
- 47. Hosono, H.; Ogo, Y.; Yanagi, H.; Kamiya, T., Bipolar Conduction in SnO Thin Films. *Electrochemical and Solid-State Letters* **2011**, *14* (1), H13.
- 48. Govaerts, K.; Saniz, R.; Partoens, B.; Lamoen, D., van der Waals bonding and the quasiparticle band structure of SnO from first principles. *Physical Review B* **2013**, *87* (23), 235210.
- 49. Quackenbush, N. F.; Allen, J. P.; Scanlon, D. O.; Sallis, S.; Hewlett, J. A.; Nandur, A. S.; Chen, B.; Smith, K. E.; Weiland, C.; Fischer, D. A.; Woicik, J. C.; White, B. E.; Watson, G. W.; Piper, L. F. J., Origin of the Bipolar Doping Behavior of SnO from X-ray Spectroscopy and Density Functional Theory. *Chem. Mat.* **2013**, *25* (15), 3114-3123.
- 50. Liang, L. Y.; Liu, Z. M.; Cao, H. T.; Yu, Z.; Shi, Y. Y.; Chen, A. H.; Zhang, H. Z.; Fang, Y. Q.; Sun, X. L., Phase and Optical Characterizations of Annealed SnO Thin Films and Their p-Type TFT Application. *Journal of The Electrochemical Society* **2010**, *157* (6), H598.
- 51. Liang, L. Y.; Liu, Z. M.; Cao, H. T.; Pan, X. Q., Microstructural, Optical, and Electrical Properties of SnO Thin Films Prepared on Quartz via a Two-Step Method. *ACS Applied Materials & Interfaces* **2010**, *2* (4), 1060-1065.
- 52. Guzmán-Caballero, D. E.; Quevedo-López, M. A.; Ramírez-Bon, R., Optical properties of p-type SnOx thin films deposited by DC reactive sputtering. *Journal of Materials Science: Materials in Electronics* **2019**, *30* (2), 1366-1373.

- 53. Wong, A.; Wang, X.; Liu, J., Nano-needle structured, ambipolar high electrical conductivity SnOx ($x \le 1$) thin films for infrared optoelectronics. *Journal of Applied Physics* **2015**, *117* (10), 103109.
- 54. Major, G. H.; Fairley, N.; Sherwood, P. M. A.; Linford, M. R.; Terry, J.; Fernandez, V.; Artyushkova, K., Practical guide for curve fitting in x-ray photoelectron spectroscopy. *Journal of Vacuum Science & Technology A* **2020**, *38* (6), 061203.
- 55. Guruvenket, S.; Hoey, J. M.; Anderson, K. J.; Frohlich, M. T.; Krishnan, R.; Sivaguru, J.; Sibi, M. P.; Boudjouk, P., Synthesis of silicon quantum dots using cyclohexasilane (Si6H12). *Journal of Materials Chemistry C* **2016**, *4* (35), 8206-8213.
- 56. Barranco, A.; Yubero, F.; Espinos, J. P.; Holgado, J. P.; Caballero, A.; Gonzalez-Elipe, A. R.; Mejias, J. A., Structure and chemistry of SiOx (x<2) systems. *Vacuum* **2002**, *67* (3), 491-499.
- 57. Martins, R.; Nathan, A.; Barros, R.; Pereira, L.; Barquinha, P.; Correia, N.; Costa, R.; Ahnood, A.; Ferreira, I.; Fortunato, E., Complementary Metal Oxide Semiconductor Technology With and On Paper. *Adv. Mater.* **2011**, *23* (39), 4491-4496.
- 58. Guzmán-Caballero, D. E.; Quevedo-López, M. A.; De la Cruz, W.; Ramírez-Bon, R., Fully patterned p-channel SnO TFTs using transparent Al₂O₃ gate insulator and ITO as source and drain contacts. *Semiconductor Science and Technology* **2018**, *33* (3), 035010.
- 59. Zhong, C. W.; Lin, H. C.; Liu, K. C.; Huang, T. Y., Improving Electrical Performances of \$p\$-Type SnO Thin-Film Transistors Using Double-Gated Structure. *IEEE Electron Device Letters* **2015**, *36* (10), 1053-1055.
- 60. Kim, S. H.; Baek, I.-H.; Kim, D. H.; Pyeon, J. J.; Chung, T.-M.; Baek, S.-H.; Kim, J.-S.; Han, J. H.; Kim, S. K., Fabrication of high-performance p-type thin film transistors using atomic-layer-deposited SnO films. *Journal of Materials Chemistry C* **2017**, *5* (12), 3139-3145.
- 61. Liang, L.; Cao, H., Ambipolar SnO Thin-Film Transistors and Inverters. *ECS Transactions* **2013**, *50* (8), 289.
- 62. Okamura, K.; Nasr, B.; Brand, R. A.; Hahn, H., Solution-processed oxide semiconductor SnO in p-channel thin-film transistors. *Journal of Materials Chemistry* **2012**, *22* (11), 4607-4610.
- 63. Reed, A.; Stone, C.; Roh, K.; Song, H. W.; Wang, X.; Liu, M.; Ko, D.-K.; No, K.; Lee, S., The role of third cation doping on phase stability, carrier transport and carrier suppression in amorphous oxide semiconductors. *Journal of Materials Chemistry C* **2020**, *8* (39), 13798-13810.
- 64. Nomura, K.; Kamiya, T.; Hosono, H., Highly stable amorphous In-Ga-Zn-O thin-film transistors produced by eliminating deep subgap defects. *Applied Physics Letters* **2011**, *99* (5), 053505.
- 65. Hsu, P.-C.; Chen, W.-C.; Tsai, Y.-T.; Kung, Y.-C.; Chang, C.-H.; Hsu, C.-J.; Wu, C.-C.; Hsieh, H.-H., Fabrication of p-Type SnO Thin-Film Transistors by Sputtering with Practical Metal Electrodes. *Japanese Journal of Applied Physics* **2013**, *52* (5S1), 05DC07.
- 66. Fahlteich, J.; Fahland, M.; Schönberger, W.; Schiller, N., Permeation barrier properties of thin oxide films on flexible polymer substrates. *Thin Solid Films* **2009**, *517* (10), 3075-3080.
- da Silva Sobrinho, A. S.; Latrèche, M.; Czeremuszkin, G.; Klemberg-Sapieha, J. E.; Wertheimer, M. R., Transparent barrier coatings on polyethylene terephthalate by single- and dual-frequency plasma-enhanced chemical vapor deposition. *Journal of Vacuum Science & Technology A* **1998**, *16* (6), 3190-3198.
- 68. Grüniger, A.; Bieder, A.; Sonnenfeld, A.; von Rohr, P. R.; Müller, U.; Hauert, R., Influence of film structure and composition on diffusion barrier performance of SiOx thin films deposited by PECVD. *Surface and Coatings Technology* **2006**, *200* (14), 4564-4571.
- 69. Sonnenfeld, A.; Bieder, A.; Rudolf von Rohr, P., Influence of the Gas Phase on the Water Vapor Barrier Properties of SiOx Films Deposited from RF and Dual-Mode Plasmas. *Plasma Processes and Polymers* **2006**, *3* (8), 606-617.

- 70. Scopece, P.; Viaro, A.; Sulcis, R.; Kulyk, I.; Patelli, A.; Guglielmi, M., SiOx-Based Gas Barrier Coatings for Polymer Substrates by Atmospheric Pressure Plasma Jet Deposition. *Plasma Processes and Polymers* **2009**, *6* (S1), S705-S710.
- 71. Xiao, P.; Lan, L.; Dong, T.; Lin, Z.; Shi, W.; Yao, R.; Zhu, X.; Peng, J., InGaZnO thin-film transistors with back channel modification by organic self-assembled monolayers. *Applied Physics Letters* **2014**, *104* (5), 051607.
- 72. Chung, W.-F.; Chang, T.-C.; Li, H.-W.; Chen, S.-C.; Chen, Y.-C.; Tseng, T.-Y.; Tai, Y.-H., H2O-Assisted O2 Adsorption in Sol-Gel Derived Amorphous Indium Gallium Zinc Oxide Thin Film Transistors. *Electrochemical and Solid-State Letters* **2011**, *14* (6), H235.
- 73. Jo, W. J.; Katsoukis, G.; Frei, H., Ultrathin Amorphous Silica Membrane Enhances Proton Transfer across Solid-to-Solid Interfaces of Stacked Metal Oxide Nanolayers while Blocking Oxygen. *Adv. Funct. Mater.* **2020**, *30* (12), 1909262.
- 74. Moore, C. W.; Li, J.; Kohl, P. A., Microfabricated Fuel Cells with Thin-Film Silicon Dioxide Proton Exchange Membranes. *Journal of The Electrochemical Society* **2005**, *152* (8), A1606.
- 75. Aoki, Y.; Muto, E.; Nakao, A.; Kunitake, T., Efficient Proton Conductivity of Gas-Tight Nanomembranes of Silica-Based Double Oxides. *Adv. Mater.* **2008**, *20* (23), 4387-4393.
- 76. Lee, J.-Y.; Lee, J. G.; Lee, S.-H.; Seo, M.; Piao, L.; Bae, J. H.; Lim, S. Y.; Park, Y. J.; Chung, T. D., Hydrogen-atom-mediated electrochemistry. *Nature Communications* **2013**, *4* (1), 2766.
- 77. de Levie, R., The electrolysis of water. *Journal of Electroanalytical Chemistry* **1999,** *476* (1), 92-93.
- 78. Carmo, M.; Fritz, D. L.; Mergel, J.; Stolten, D., A comprehensive review on PEM water electrolysis. *International Journal of Hydrogen Energy* **2013**, *38* (12), 4901-4934.
- 79. Zhang, H.; Weiss, I.; Rudra, I.; Jo, W. J.; Kellner, S.; Katsoukis, G.; Galoppini, E.; Frei, H., Controlling and Optimizing Photoinduced Charge Transfer across Ultrathin Silica Separation Membrane with Embedded Molecular Wires for Artificial Photosynthesis. *ACS Applied Materials & Interfaces* **2021**, *13* (20), 23532-23546.
- 80. Van de Walle, C. G., Hydrogen as a Cause of Doping in Zinc Oxide. *Physical Review Letters* **2000**, *85* (5), 1012-1015.